Additive Manufacturing 17 (2017) 23–38

Contents lists available at ScienceDirect

Additive Manufacturing

journal homepage: www.elsevier.com/locate/addma

Full Length Article

Investigation of pore structure in cobalt chrome additively manufactured parts using X-ray computed tomography and three-dimensional image analysis☆

F.H. Kim[a,*], S.P. Moylan[a], E.J. Garboczi[b], J.A. Slotwinski[c]

[a] *National Institute of Standards and Technology, Intelligent Systems Division, Gaithersburg, MD, USA*
[b] *National Institute of Standards and Technology, Applied Chemicals and Materials Division, Boulder, CO, USA*
[c] *The Johns Hopkins University, Applied Physics Laboratory, Laurel, MD, USA*

ARTICLE INFO

Article history:
Received 23 December 2016
Received in revised form 11 May 2017
Accepted 27 June 2017
Available online 15 July 2017

Keywords:
Additive manufacturing
Metal
Porosity
X-ray computed tomography
Image analysis

ABSTRACT

Pore structures of additively manufactured metal parts were investigated with X-ray Computed Tomography (XCT). Disks made of a cobalt-chrome alloy were produced using laser-based powder bed fusion (PBF) processes. The additive manufacturing processing parameters (scan speed and hatch spacing) were varied in order to have porosities varying from 0.1% to 70% so as to see the effects of processing parameters on the formation of pores and cracks. The XCT images directly show three-dimensional (3D) pore structure, along with cracks. Qualitative visualization is useful; however, quantitative results depend on accurately segmenting the XCT images. Methods of segmentation and image analysis were carefully developed based, as much as possible, on aspects of the images themselves. These enabled quantitative measures of porosity, including how porosity varies in and across the build direction, pore size distribution, how pore structure varies between parts with similar porosity levels but different processing parameters, pore shape, and particle size distribution of un-melted powder trapped in pores. These methods could possibly serve as the basis for standard segmentation and image analysis methods for metallic additively manufactured parts, enabling accurate and reliable defect detection and quantitative measures of pore structure, which are critical aspects of qualification and certification.

Published by Elsevier B.V.

1. Introduction

Additive Manufacturing (AM) is a revolutionary manufacturing technique for creating complex geometry parts. Various materials (polymer, ceramic and metal), different techniques (laser and electron beam melting and extrusion) and processes (powder bed fusion and direct energy deposition) are now used in AM. This paper focuses on metal-based AM, which has great potential in a wide range of industries including aerospace, automotive, and medical implants. For widespread adoption of this technology, however, thorough characterization of microstructure as related to performance is needed. "Microstructure" can mean both grain-level crystallography and grain-level orientation statistics, as well as larger length-scale pore structure and cracks. "Larger length-scale" is defined here as equal to or larger than the smallest metal powder particle, in this case around 10 μm, and is the focus of our paper, since the X-ray Computed Tomography (XCT) instrument used was limited to a resolution of a few micrometers. Quantification of pore structure can be for the purpose of quality control in eliminating pores, or for quality control in producing a desired pore structure and/or pore size distribution, for example in porous biological implants.

Pores are commonly observed in AM parts. Pores in AM can be characterized as lack-of-fusion pores and gas pores. Lack-of-fusion pores generally occur due to incomplete melting and generally have irregular shapes and can contain sintered but un-melted powders [1]. Gas pores probably occur due to pores within the original metal powder produced with a gas atomization process [2–5] or trapping gas in the environment, and they are roughly spherically-shaped. The exact cause of these pores is still under discussion [6]. Both types of pore can occur simultaneously in a part [7] and both can affect mechanical properties [8]. Critical pore size and structure are yet to be determined for AM, and of course will depend on expected mechanical properties in service, but are thought to be on the order of 100 μm for typical applications. Pores with angu-

☆ Official contribution of the U.S. National Institute of Standards and Technology – Not subject to copyright in the United States.

* Corresponding author.
E-mail address: felix.kim@nist.gov (F.H. Kim).

http://dx.doi.org/10.1016/j.addma.2017.06.011
2214-8604/Published by Elsevier B.V.

Table 1
Processing parameters and porosity measurements of CoCr disks.

Sample	Hatch speed, v (mm/s)	Hatch spacing, h (mm)	Energy density, E (10^9 J/m^3)	Porosity[a] φ_w (%)
1	800	0.1	121.9	0
2	1600	0.1	60.9	1.4
3	3200	0.1	30.5	18.1
4	800	0.2	60.9	2.1
5	800	0.4	30.5	10.2
6	3200	0.4	7.6	72.0

[a] Measured by manufacturer via mass and volume measurement.

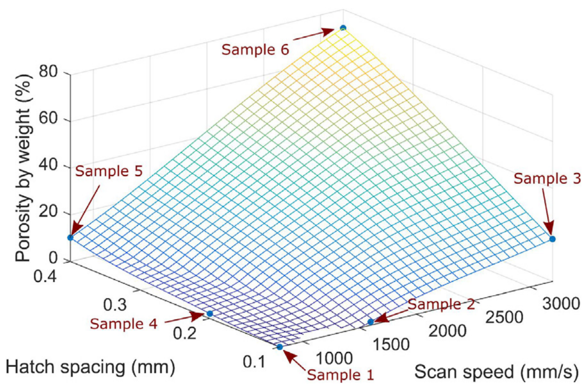

Fig. 1. Processing parameters and porosity.

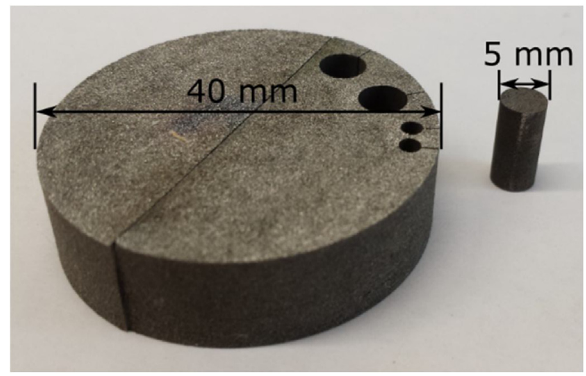

Fig. 2. CoCr disk and cored cylinder.

lar shape are expected to affect mechanical properties more than spherically-shaped pores, due to greater stress concentration at the tips. While porosity is typically measured with gravimetric techniques or Archimedes' method, the actual pore structure and pore distribution has not been thoroughly considered, although preliminary attempts have been made [9,10]. Characterization of pore structure in 3D is crucial for determining macroscopic properties for any heterogeneous material [11], including AM materials.

Conventional imaging techniques, such as optical microscopy, provide 2D information of outer surfaces or inner surfaces via cross-sectioning. Serial sectioning and subsequent microscopy can evaluate three-dimensional microstructure; however, the sample is destroyed by the serial sectioning process. Out of many non-destructive evaluation techniques (e.g., ultrasound testing, eddy current), XCT provides clear microstructural information in three-dimensions (3D) and so is a promising candidate for imaging AM-produced components [12].

Initially used in medical imaging starting in the 1970s, XCT has since been applied to study various materials including geomaterials, biomaterials, polymers, metals, and advanced materials [13]. Porous media such as soils and foams have been characterized with XCT [14–16]. Metallic samples generally require higher-energy X-rays for sufficient transmission. For clear images, typically around 25% of the X-ray photons need to pass through the sample based on experience, but significantly smaller (3%) or larger (90%) transmission can still allow successful CT reconstruction. We chose 10% transmission as the minimum required value to obtain reliable XCT data, which required a 155 kV tube voltage, close to the maximum value obtainable for the instrument. Increasing tube voltage generally results in lower contrast between phases, but in this case, metal vs. pores, the phase contrast was adequate. Characterization of pores occurring in conventional metal casting has also been performed with XCT [17,18]. XCT-based research of metal AM-produced parts is still limited, although synchrotron-based CT analysis of porosity in a metal matrix composite has been carried out [19].

In this paper, we used XCT to study the pore structure of AM parts, including the effect of AM processing parameters. While a few of the XCT images studied here were also examined in an earlier publication [9], in this paper a more in-depth analysis of the pore structure was performed with additional images and more careful image analysis. This study is also presented as an example of how to carefully select image processing parameters and image segmentation algorithms, which are required for valid quantitative analysis, based on aspects of the images themselves. It is hoped that this paper can serve as a basis for developing standardized analysis of XCT images of AM parts.

Table 2
Image information for XCT scans.

Sample	Voxel Size (μm)	Volume (voxel)	Volume (mm^3)
2	2.45	980 × 1010 × 1000	2.40 × 2.47 × 2.45
3	2.77	988 × 1013 × 990	2.74 × 2.81 × 2.75
3 high-res	0.89	956 × 1012 × 995	0.85 × 0.90 × 0.89
4	2.43	984 × 1010 × 1000	2.39 × 2.45 × 2.43
5	2.52	984 × 1010 × 1000	2.48 × 2.55 × 2.52
5 high-res	0.87	984 × 1009 × 851	0.86 × 0.88 × 0.74
6	2.77	984 × 1013 × 990	2.73 × 2.81 × 2.75

2. Materials and methods

Cobalt-chrome alloy (expected chemical elements: Co, Cr, Mo, Si, Mn, Fe, C, and Ni) disks were produced using laser-based powder bed fusion (PBF) processes (EOS M270 Direct Metal Laser Sintering System (DMLS)[1]) with varying scan speed (straight line speed of laser), varying hatch spacing (the distance between adjacent laser scanning tracks), a constant laser power of 195 W, and a nominal distance between build layers of 20 μm. Pre-alloyed and gas-atomized CoCr powders, with size, as measured by laser diffraction, between 5 μm and 80 μm, with a peak around 30 μm, were

[1] Certain commercial equipment, instruments, or materials are identified in this paper in order to specify the experimental procedure adequately. Such identification is not intended to imply recommendation or endorsement by the National Institute of Standards and Technology, nor is it intended to imply that the materials or equipment identified are necessarily the best available for the purpose.

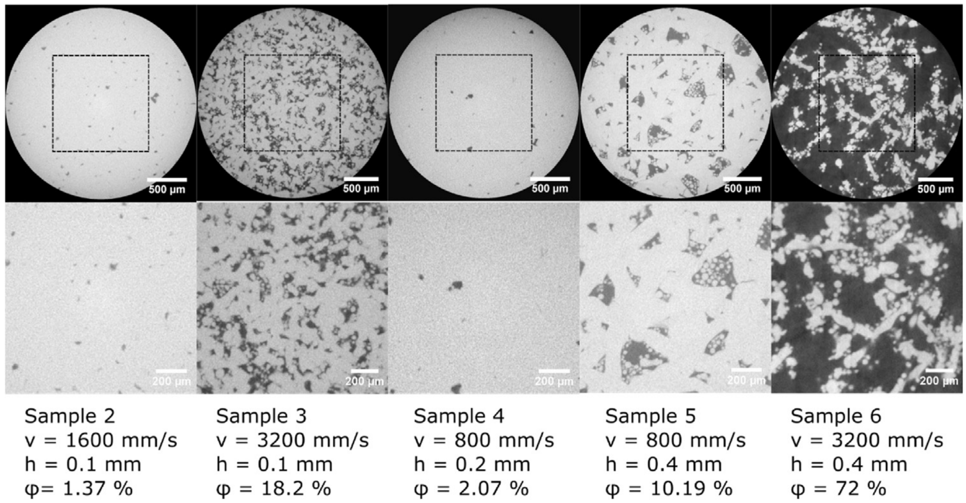

Fig. 3. Typical XCT images of five samples produced with different AM processing parameters.

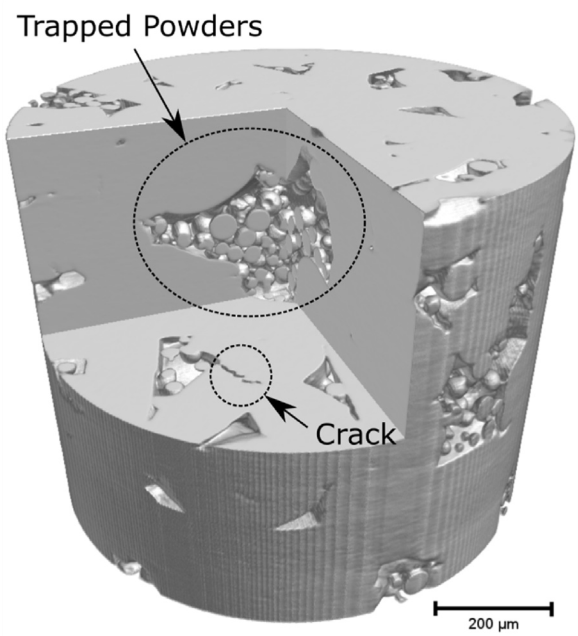

Fig. 4. High-resolution (0.87 µm/voxel) image of cracks and trapped powders in Sample 5.

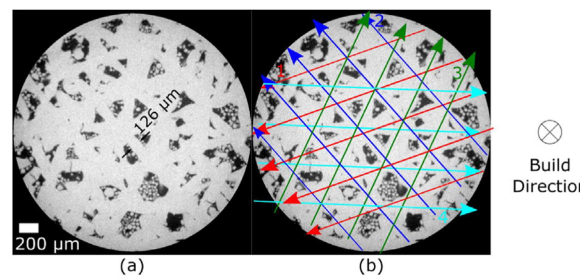

Fig. 5. Example measurement of (a) hatch thickness and (b) identification of hatch direction and the number of laser energy inputs (red, blue, yellow, green) that affected the pore structure at the same height in the build direction. (For interpretation of the references to colour in this figure legend, the reader is referred to the web version of this article.)

used [20]. The as-built CoCr disks were 40 mm in diameter and 10 mm in height, with no post-processing step (e.g. heat treatment or hot isostatic pressing) used. The porosities of the disks (φ_W) were computed from total mass and volume measurements, using the known value of the density of the solid metal alloy. The processing parameters, energy density, and porosity are provided in Table 1. The bulk porosities of all six samples listed in Table 1 were measured by the manufacturer. The measured porosity values are graphically visualized in Fig. 1 as a function of hatch speed and spacing. The values of these parameters were chosen so as to obtain a wide range of porosities. Only one sample achieved close to full density, a porosity of 0.003%, which was not examined in this study since it only contained a few pores. In Fig. 1, the measured porosity monotonically increases with both increasing hatch speed and spacing. The energy density is a measure of the energy applied per volume of material during the scanning of a layer, as shown in Eq. (1), where P is the laser power (in J s^{-1}), v is the scanning velocity (m/s), h is the hatch spacing (m) and t is the layer thickness (m) [21]:

$$E = \frac{P}{v \cdot h \cdot t} \qquad (1)$$

The energy density has been known to affect the value of the global porosity [22], but the resulting pore structure has not been investigated thoroughly. It is interesting to note that Samples 2 and 4 have the same energy density input, and Samples 3 and 5 also have the same energy density input, different from Samples 2 and 4. While the global porosity values may be similar for these sample pairs with the same energy density input, the pore structure can be quite different, as will be shown.

The XCT measurements were made using the NIST ZEISS Versa XRM500 system. A 155 kV voltage and 10 W of power were used for the XCT imaging, along with the highest X-ray attenuation filter available for the instrument, in order to harden the beam spectrum and increase transmission to the required 10%. The actual filter material and thickness were proprietary information of the manufacturer. Five mm diameter cylinders were cored out of each disk (Fig. 2) as explained in Slotwinski et al. [9]. The XCT system is composed of a microfocus X-ray source (30 kV–160 kV), rotary stage, and a charge-coupled device (CCD) camera (13.5 µm/pixel) with exchangeable lenses with various magnifications. This XCT instrument uses both geometrical magnification and optical lens magnification. Two settings were used, which resulted in images with pixel sizes ≈2.44 µm and ≈0.87 µm. While there were 2048 × 2048 pixels available in the CCD camera, a pixel binning (2 × 2) was applied to use 1012 × 1012 pixels that

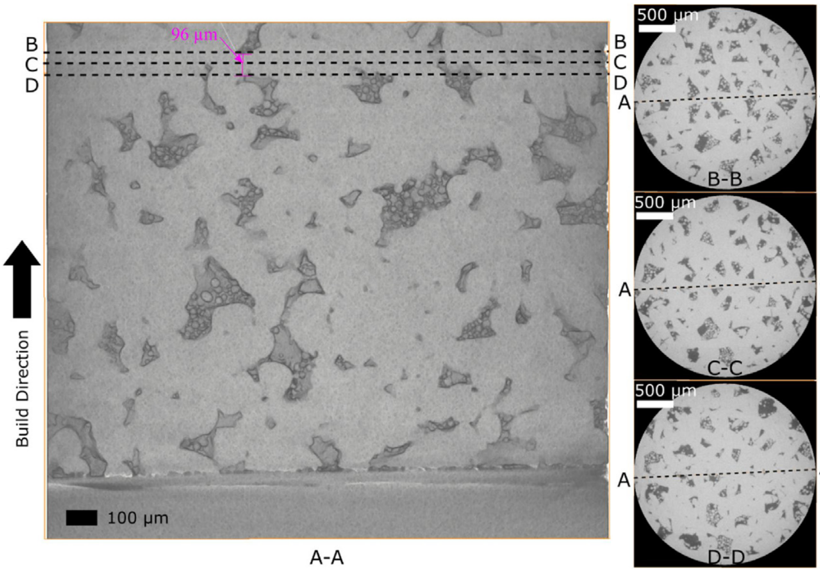

Fig. 6. Visualization of depth of laser melt in Sample 5.

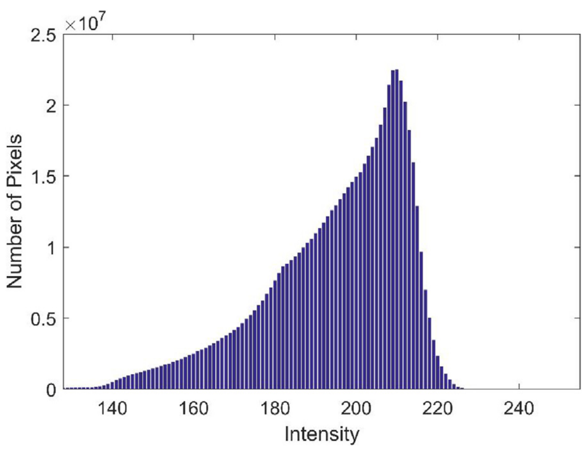

Fig. 7. Histogram of Sample 2.

had four times the area in order to improve signal-to-noise ratio. Typical cone-beam CT reconstruction was performed with the XCT system manufacturer software. No pre-processing, no ring removal, and no beam hardening correction were performed. A smoothing filter (Kernel Size: 0.7) was applied during the filtering process. After CT reconstruction, approximately $1000 \times 1000 \times 1000$ voxel 3D images were obtained, for an actual volume of about $(\pi/4)$ $(2.5\,\text{mm})^3$ in case of the approximately 2.5 μm voxel data sets. XCT scans with a pixel size of 0.87 μm were also obtained for Samples 3 and 5 only, using different cylinders than used for the 2.44 μm/voxel images, as shown in Table 2. A CT scan of Sample 1 was acquired but not studied, as there were very few observable pores in this image set. Cylindrical sub-volumes of the 5 mm diameter cylinders were obtained by using the local or interior tomography technique [23].

3. Results: qualitative

3.1. Processing parameters and microstructure

Typical reconstructed images of Samples 2 through 6 are compared in Fig. 3. Major differences in the pore structure are seen between the parts produced with different processing parameters. As listed in Table 1, Samples 2 and 4 received the same energy density input from different processing parameters, which produced similar porosity levels. Compared to Sample 4, Sample 2 appears to have a larger number of pores that are smaller in size, but neither appears to contain trapped powder particles. Samples 3 and 5 also have similar total porosities, but their pore structures seem quite different from each other, and both samples do contain un-melted powder particles. Compared to Sample 5, there is a larger number of individual pores that appear better connected in Sample 3. Fewer but larger pores are observed in Sample 5. Clearly, the pore structure of a build cannot be characterized based on porosity value alone. Due to a large hatch spacing, many un-melted powder particles are observed in the larger Sample 5 pores, although there are also some visible in the smaller Sample 3 pores. These powders contribute to the mass-based density measurement, but contribute little to the mechanical performance, especially in tension.

Sample 6 was manufactured to have a very high porosity, about 72%. The solid framework in Sample 6 looks to be disconnected in 2D, but that is an artifact. In 3D, the solid framework is really connected, since the entire sample held together mechanically. The difference between 2D and 3D is related to the fact that percolation thresholds are generally lower in 3D than in 2D [24]. A percolation threshold for a pore space is the critical porosity above which a porous medium is connected in 3D. If the solid volume fraction of a 3D percolated structure is less than the relevant 2D percolation threshold in terms of area fraction, a 2D cross-section of the 3D percolated structure, which is known to have an area fraction equal to the 3D volume fraction via stereology [25], may appear to be unpercolated.

3.2. Trapped powder

In Sample 3, a large number of small individual pores was observed. At the contacts, many powder particles appear to be partially melted, possibly due to the balling effect. Balling is formations of ellipsoidal or spherical balls with size of 10 μm–500 μm due to surface tension in high oxygen content or low energy input (high scan speed or low laser power) [26]. In Sample 5, individual pores are fewer and larger than in Sample 3, and the laser tracks are much more obvious than in Sample 3. Within these large pores, a significant amount of powder is trapped, as shown in Fig. 4, which is a smaller voxel enlarged view of part of Sample 5.

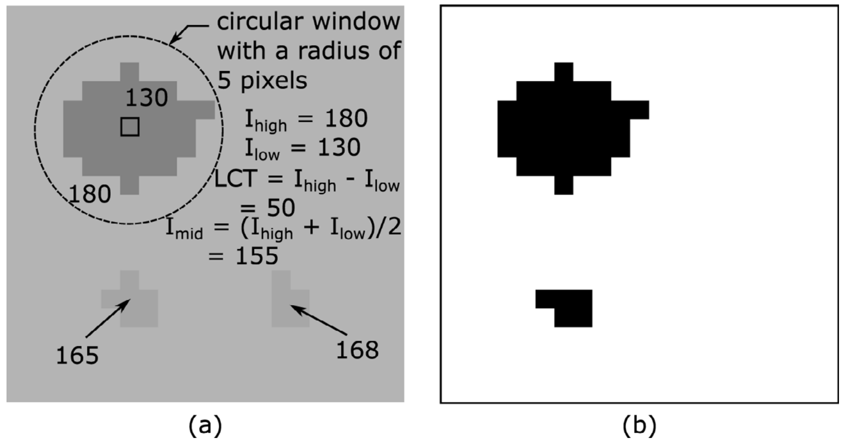

Fig. 8. a) An artificial image of three pores of different sizes with a local threshold circular window applied around the marked pixel in the I = 130 pore; b) the same image thresholded by application of Bernsen's method using DCT = 15.

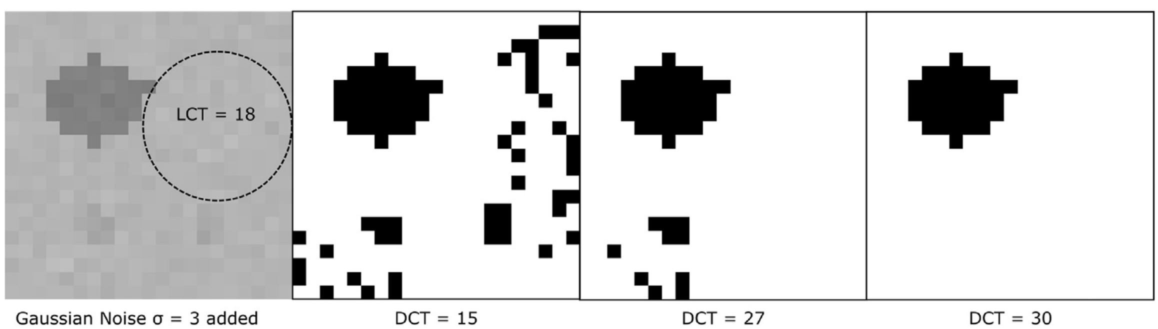

Fig. 9. The effect of noise on proper choice of local contrast value.

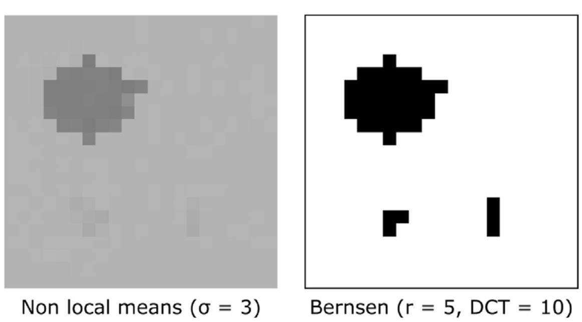

Fig. 10. a) Effect of non-local means filter on the image from Fig. 9, with added Gaussian noise and b) result of on Bernsen local thresholding on the image.

3.3. Cracks

Cracks are known to be formed due to thermal stresses as melted metal solidifies and cools. It has been reported that cracks generally form at part edges due to thermal and residual stress [27]. The cylindrical samples are cored from the disk samples, and the XCT scans done here were interior scans, or "virtual cores", so they do not show part boundaries. While other samples do not clearly show any sign of cracks, cracks are clearly observed in the high-porosity Sample 5 through individual hatches. Cracks appear to occur where different hatches cross each other, as can be seen in Fig. 4.

3.4. Effect of hatch rotation on structure

The result of processing strategies such as hatch rotation can be observed by analyzing Sample 5 with the approximately 2.5 μm/voxel data set. The pore structure in the cross-sectional image is a result of laser energy depositions of several layers. The 195 W laser can melt hundreds of micrometers of metal powders, which covers many build layers, since the nominal build layer thickness was 20 μm. The AM machine used for this research rotated the laser scanning direction 67° for each layer. Due to a large hatch spacing, the individual laser tracks can be easily identified. For this particular location, at least four different hatch directions can be identified, which indicates that energy deposition from four different layers generated the structure seen in this 2.5 μm-thick image. Therefore, in some areas, the process of melting and rapid solidification occurred at least four times. The image in Fig. 5a shows the pore structure with multiple solidified laser tracks. One of the tracks was measured to be about 126 μm wide, which is larger than the nominal laser spot size of 100 μm, similar to the observation of Yadroitsev et al. [28]. For this particular location, based on Fig. 5b, we can see the laser melted metal and powder from about four layers, which means a linear distance of 80 μm, since each layer was nominally 20 μm. The four laser scan tracks are shown with four different color arrows, and the laser tracks of subsequent layers are approximately 67° apart. By looking at a vertical (build direction) slice of the XCT scan, it is possible to measure the depth of laser energy deposition, as shown in Fig. 6. The vertical slice is through a single hatch (labelled A-A) obtained by rotating a typical vertical orthoslice to the angle of the particular hatch orientation, and three cross-sectional CT slices, separated by approximately 48 μm in the build direction, are shown from top to bottom of the hatch (slices B-B, C-C, D-D). The hatch depth was measured to be about 96 μm, which is an estimate of how deep the laser energy was deposited for the given processing parameters.

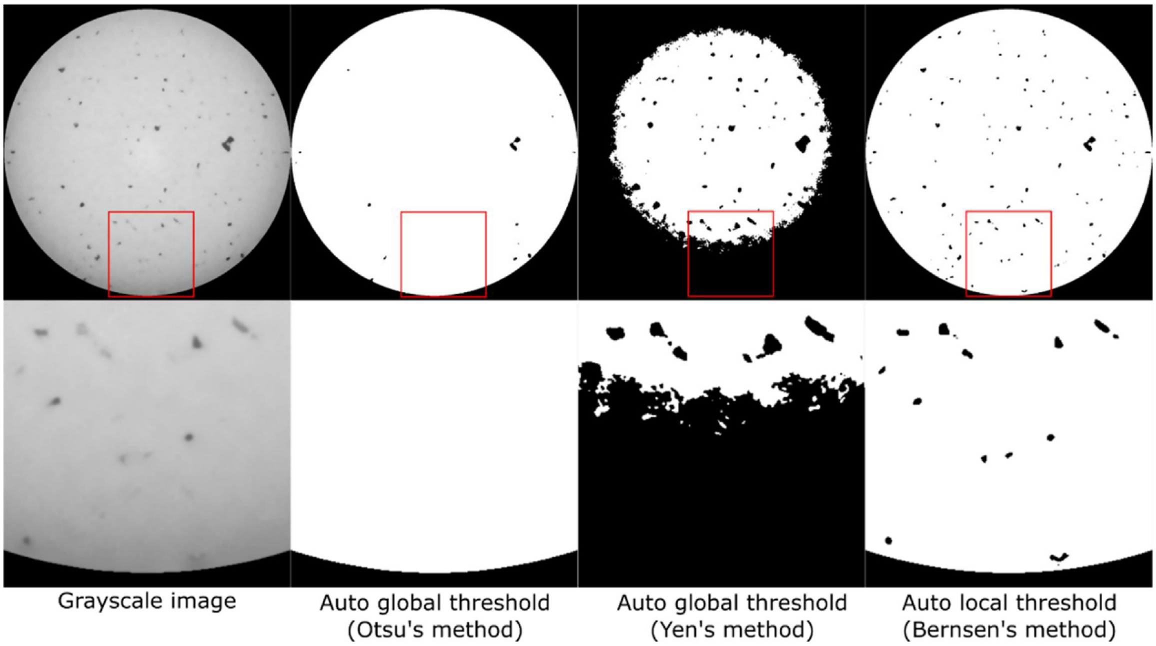

Fig. 11. Comparison of automatic global threshold and automatic local threshold results of an XCT image.

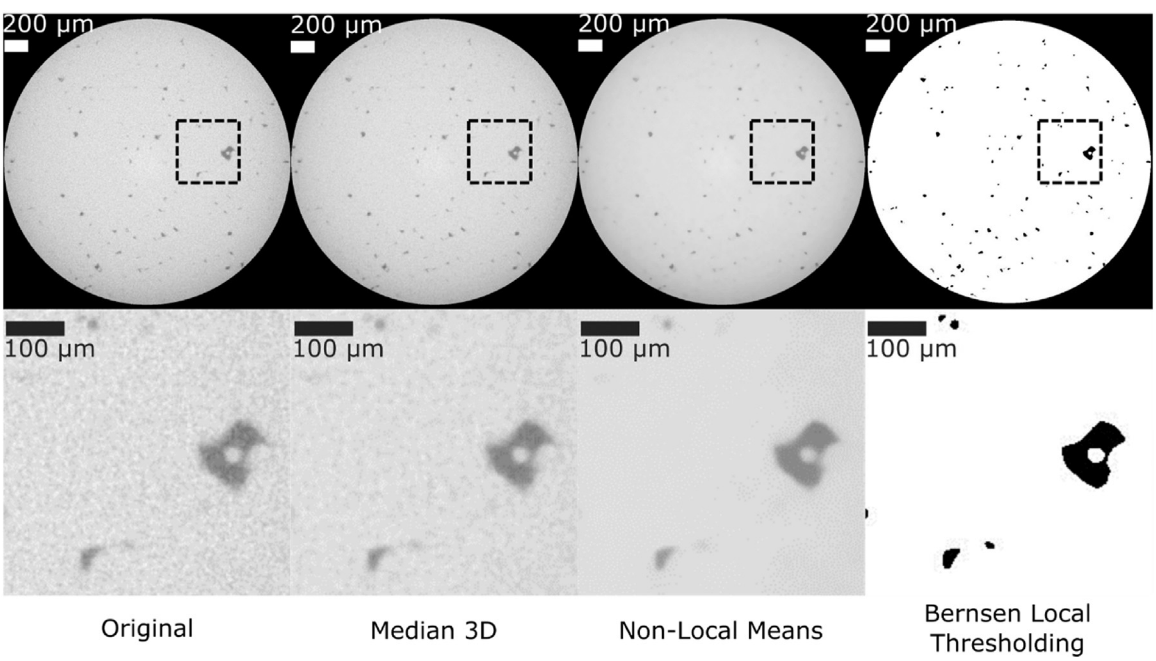

Fig. 12. Image processing and thresholding steps shown on a CT image of Sample 2.

4. Image processing and thresholding

Quantitative study of XCT gray-scale images of metallic AM parts requires a series of image processing steps ending in a thresholding/segmentation process, in which metal is changed to a single gray scale (e.g. white) and pores are changed to a different gray scale (e.g. black) [29]. The fidelity of the binary image with the original gray scale images and the number of image processing steps necessary are dependent on the original XCT image quality. A good XCT scan should have a high signal-to-noise ratio of individual projection images, an adequate number of projection images for accurate reconstruction, and adequate X-ray contrast of the material phases present. The choice of reconstruction algorithm and the extent of smoothing that may be applied during the filtering process of the usual commercial filtered back-projection algorithm could also affect the XCT image quality. Depending on the image quality, a few image processing steps can be applied to reduce noise, and the choice of algorithms and the sequence of application are important. The best choices of algorithm are debated among researchers, and in general depend on the system analyzed. Some additional image processing algorithms such as a morphological filter may be applied to further segment parts or remove regions inaccurately segmented due to noise. Overall, image processing in XCT image analysis is quite complicated, and no set of standard rules have been established. In this paper, the effects of image processing on measurement of porosity and pore size distribution are presented and

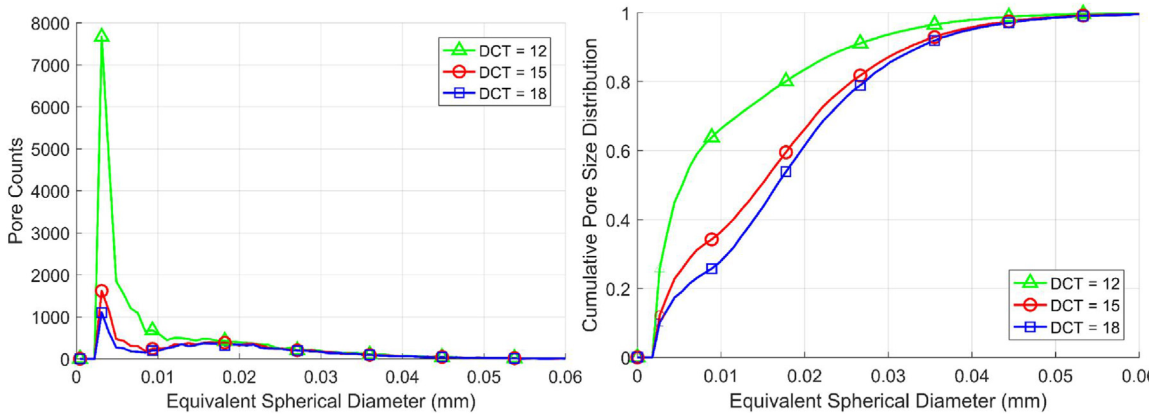

Fig. 13. Effect of DCT value on pore size distribution and cumulative pore size distribution of Sample 2.

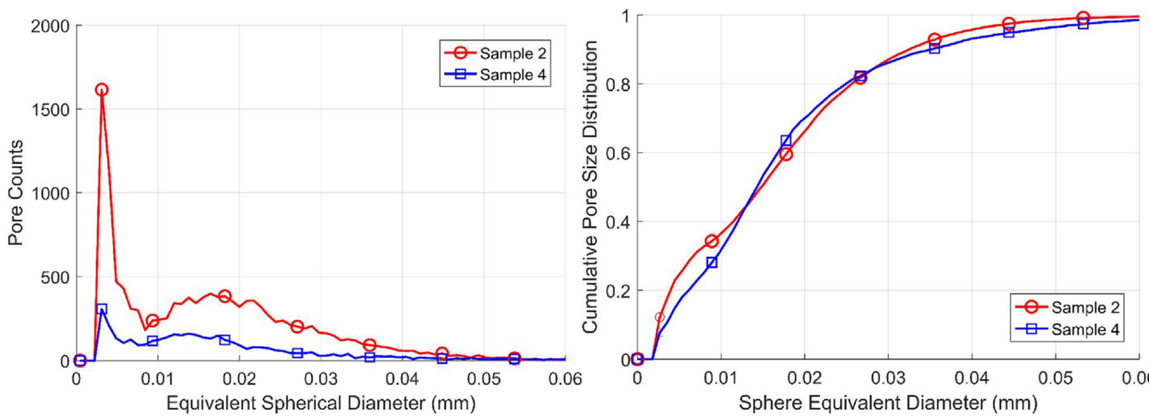

Fig. 14. Pore size distribution and cumulative pore size distribution comparisons of Sample 2 (DCT = 15) and Sample 4 (DCT = 21).

discussed to provide steps toward possible standard image analysis methods for these specific materials.

Non-uniformity in gray scale intensity in the nominally uniform metal solid phase is observed in XCT images due to the polychromatic spectrum of the typical laboratory X-ray tube source. A synchrotron source can provide a much more monochromatic spectrum and so can reduce this noise. This non-uniformity in gray scale in what is clearly metal makes it difficult to properly segment the entire image using only a single gray-scale threshold, which can artificially remove or create pores. The gray-scale histogram of sample 2 in Fig. 7 does not show distinct peaks for the pore phase, which is an indication of the non-uniform gray scales in the images. For this reason, an automatic local thresholding algorithm using Bernsen's method [30,31], as implemented in the ImageJ open-source software [32], was used for the various 2D images with some success.

The local thresholding processes were performed in local windows of a predetermined size (user-chosen) for every pixel in each 2D XCT image. The diameter of the local window should be larger than the largest pore, but the window radius should be smaller than the smallest distance between two different pores, if possible. The threshold condition is evaluated for the local window surrounding each pixel, and the value of the pixel of interest is converted to either 0 (pore) or 1 (solid). A circular window with a radius of 5 pixels was used for the following examples and for the actual results in this paper.

In the algorithm, *I(i,j)* is the gray scale value of the pixel at the location *(i,j)*, and *B(i,j)* is the new value at the pixel of interest, either 0 or 1, after the algorithm is applied. We are assuming we are working with 8-bit images, so the maximum gray scale is 255, the minimum value is 0, and the mid-level value is 128. If other size images are used, they can be converted to 8-bit images. The version of Bernsen's algorithm we used assumes that the matrix or solid phase has gray scale values greater than 128. If a given image does not meet this criterion, it should be appropriately rescaled. The local contrast threshold, LCT, is the positive difference between the maximum (I_{high}) and the minimum (I_{low}) gray scale value within a given window, and I_{mid} is their arithmetical average. The default contrast threshold, DCT, is a user-defined parameter of the algorithm, which can be determined automatically based on information contained in the images themselves. The algorithm is the following: If LCT < DCT, then

$$B(i,j) = \begin{cases} 1, I(i,j) > 128 \\ 0, I(i,j) \leq 128 \end{cases}$$

If LCT ≥ DCT, then

$$B(i,j) = \begin{cases} 1, I(i,j) > I_{mid} \\ 0, I(i,j) \leq I_{mid} \end{cases}$$

The key to an accurate thresholding process is clearly the choice of DCT, once an appropriate size window is chosen based on apparent pore size and pore spacing.

An artificial XCT image was created to better illustrate how this local thresholding process works (Fig. 8). Three pores (dark) exist within the solid background (light). The solid has gray level of 180 and the largest pore has gray level of 130. The two smaller pores have gray values of 165 (left pore) and 168 (right pore). The pores have lower gray values than the solid, but as the pore size decreases, the gray scale value increases and becomes closer to that of the solid, which tends to be the case in real XCT images, due to the

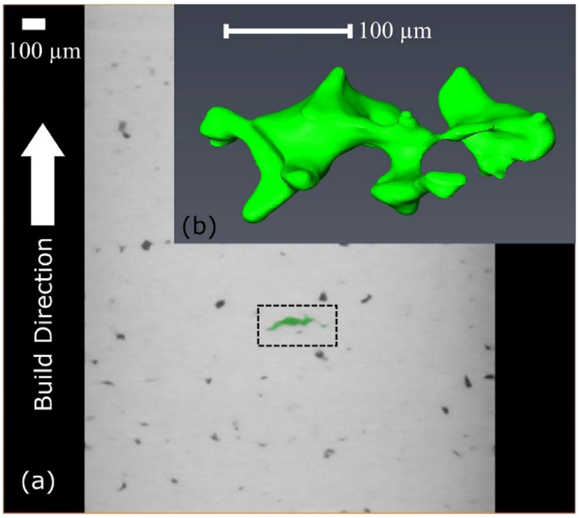

Fig. 15. The largest pore (a) location and (b) shape.

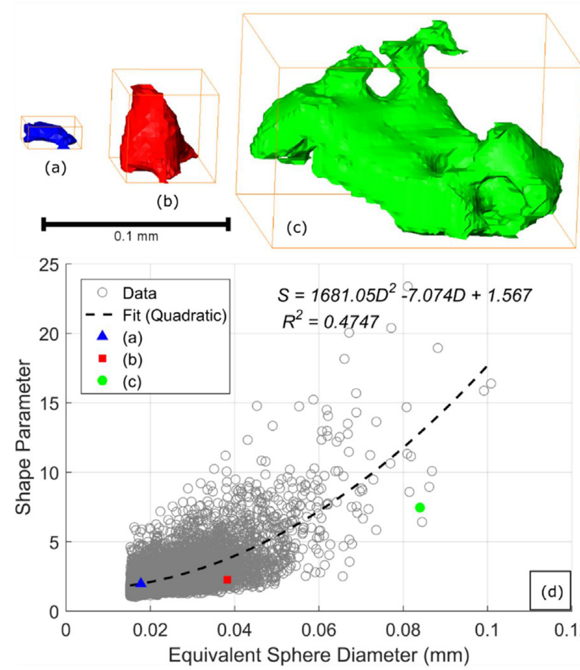

Fig. 16. Example 3D visualization of pore shapes (Top) and comparison of pore shape and size of pores with a graph (Bottom).

reconstruction process which tends to blur together gray scales on either side of a phase boundary.

A circular window of radius 5 pixels was generated for the pixel marked with a hollow square in the middle of the largest pore in Fig. 8a, and the value of DCT was chosen to be 15. For this window, I_{high} = 180, I_{low} = 130, so that LCT = 50 and I_{mid} = 155. Since LCT = 50 > DCT = 15 and the gray scale value of the pixel of interest, I = 130, is lower than I_{mid} = 155, therefore, this pixel is thresholded to 0. The process can be repeated for every pixel in Fig. 8a, with the resulting image shown in Fig. 8b. The pixels in the smallest pore, which have LCT = 12, were not converted to 0 since DCT = 15 was larger than this value and I = 130 was larger than 128. This illustrates the need to select the value of DCT to be smaller than the LCT value for the smallest pore in the image, so that all identifiable pores remain pores after the thresholding process. Scanning the image and finding the lowest LCT value is then one way to guide the choice of the DCT value, based on the images themselves.

A better way for choosing the value of DCT is to make DCT to be some multiple of the average gray scale standard deviation in the matrix phase. This method is preferred, since it is computationally much easier, and will be used for the actual XCT images. To illustrate this method, Gaussian noise with a standard deviation of 3 was added to the image in Fig. 8a. The resulting gray-scale image is shown in Fig. 9. Due to the added noise, the LCT value for the matrix window shown in the left side of Fig. 9 now changes to 18 but would have previously been 0 in the uniform matrix. Keeping DCT = 15 results in some artificial pores, as shown in the next image in Fig. 9. Increasing the value of DCT in the final two images in Figs. 9–27 and then to 30 removes these artificial pores but also removes the two smaller pores that were in the image, since these now have a lower contrast with the solid matrix.

One way to get around the problem of noise in what should be a uniform phase like the solid matrix is to use a non-local means filter [33]. Since Gaussian noise of standard deviation 3 was added to the image, one should apply a non-local means filter to the noisy image that also has a standard deviation of 3, which would approximately remove the noise. A non-local means filter, available as a plugin for ImageJ, was used for this example [34]. In a real image, the standard deviation to be used in the non-local means filter would be the computed gray scale standard deviation in the nominally uniform area, which is easily computed and used. Again, the correct parameters of the image analysis process can be derived from the images themselves.

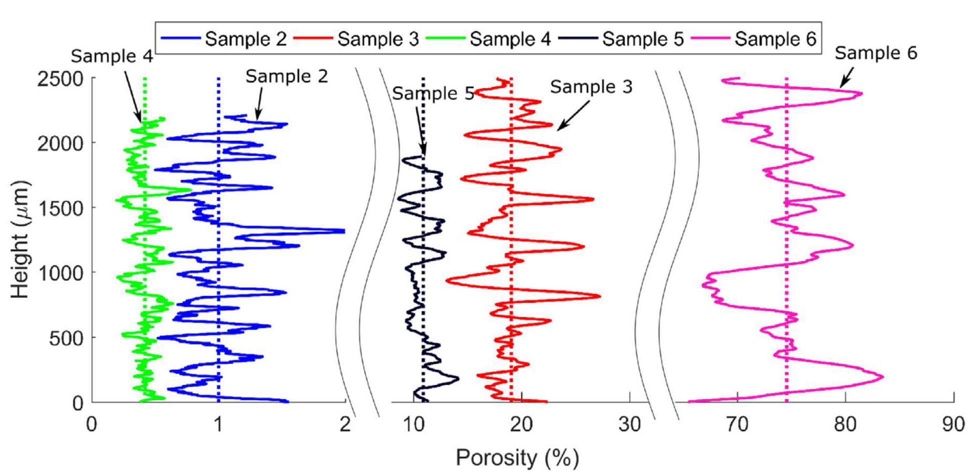

Fig. 17. Variation of porosity over height (dotted lines are global porosity values).

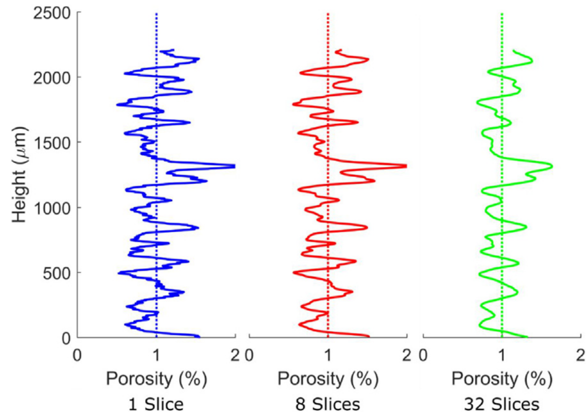

Fig. 18. Slice-wise porosity and the effect of slice averaging over height of Sample 2. The dashed lines indicate the Sample 2 global porosity.

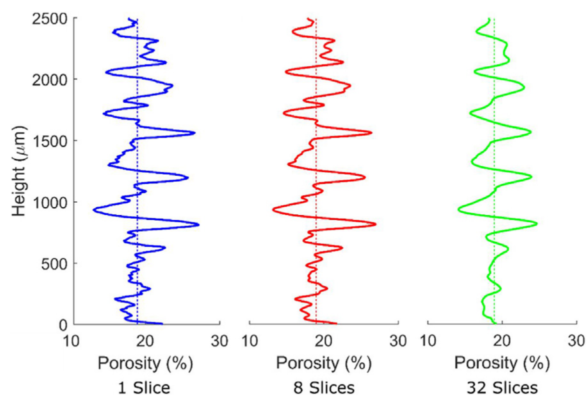

Fig. 19. Slice-wise porosity and the effect of slice averaging over height of Sample 3. The dashed lines indicate the Sample 3 global porosity.

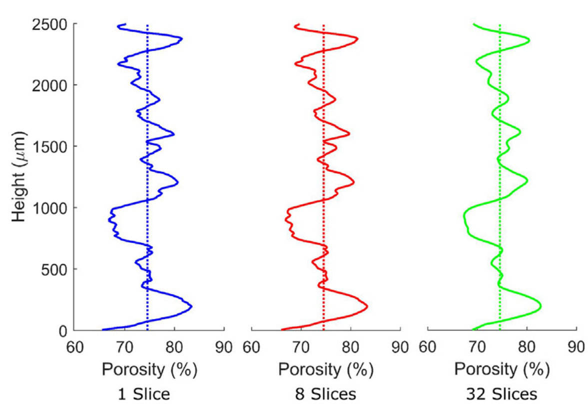

Fig. 20. Slice-wise porosity and the effect of slice averaging over height of Sample 6. The dashed lines indicate the Sample 6 global porosity.

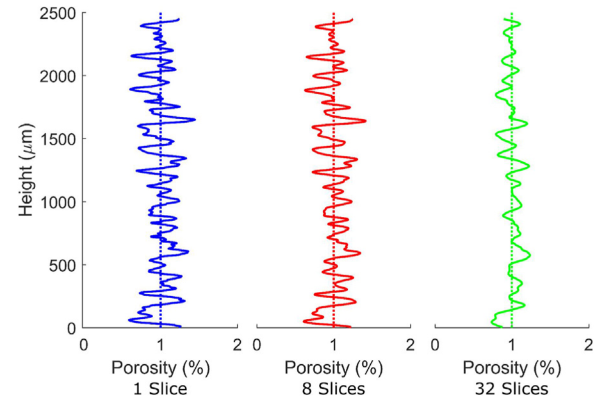

Fig. 21. z-layer porosity and the effect of slice averaging over height of Sample 2 model, where monosize spheres of diameter 61 μm were used.

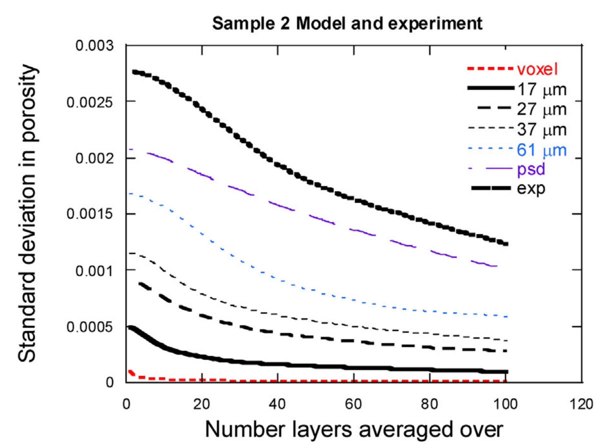

Fig. 22. A plot illustrating how the standard deviation in the porosity, computed over the build direction, varies with the number of layers considered in the running average.

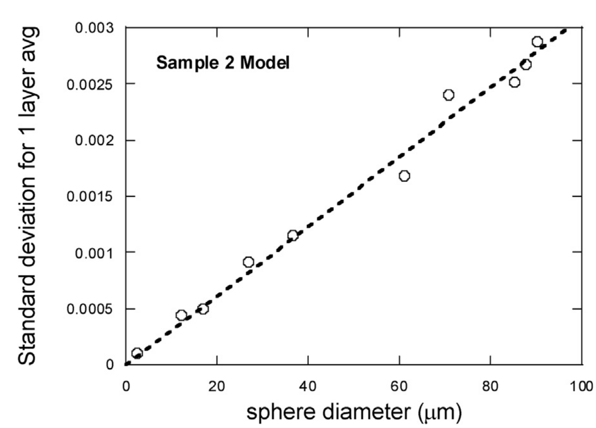

Fig. 23. The 1-layer porosity standard deviation in the build direction, vs. the sphere diameter for the spherical pore models.

Fig. 10 shows Fig. 9 image after the filter has been applied (left) and the binary image (right) that comes from Bernsen's local thresholding algorithm. Some accuracy is lost for the pores, but all three pores are at least represented in the final binary image, unlike in Fig. 9. Now we consider application of Bernsen's local thresholding algorithm to a real XCT image from the Sample 2 image set. Smoothing algorithms (a 3D $3 \times 3 \times 3$ median filter and a non-local means filter) were already applied. The standard deviation parameter for the non-local means filter was obtained from the image itself as described above. As was previously mentioned, the standard deviation of gray values within a local window (radius = 5 pixels) can be used as a basis for determining a proper DCT value. Standard deviations, within local windows, were measured at five different locations (top, bottom, left, right, and center) within a single XCT slice, and the process was repeated for three different CT slices at the top, middle, and bottom of the XCT stack, where the local windows fully covered uniform solid areas. The standard deviation of the histogram is related to the fluctuation of image intensity, and this varies within a CT slice and over the entire image stack.

The measured standard deviations are shown in Table 3. The overall average of the 15 data points was 0.847. Assuming that the image histogram follows a normal distribution, choosing the DCT

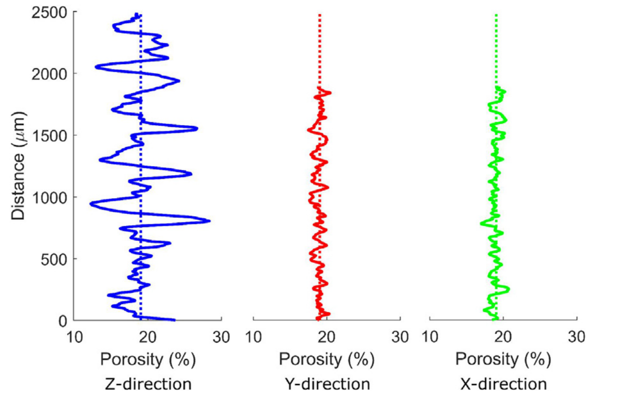

Fig. 24. Distance vs. porosity for Sample 3 for the x, y, and z directions, computed on a $684 \times 684 \times 900$ sub-sample of the original thresholded image stacks.

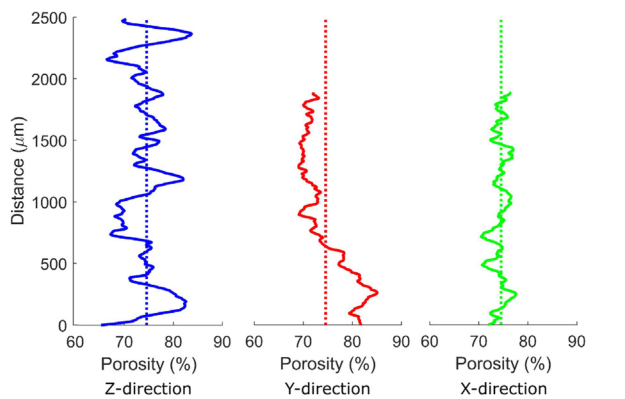

Fig. 25. Distance vs. porosity for Sample 6 for the x, y, and z directions, computed on a $684 \times 684 \times 900$ sub-sample of the original thresholded image stacks.

Table 3
Standard deviation measurement of Sample 2.

	Bottom Slice	Middle Slice	Top Slice
Left	0.816	0.732	1.128
Right	0.607	0.986	1.492
Top	0.948	0.38	0.902
Bottom	0.723	0.68	0.969
Center	1.126	0.777	0.433

larger than almost 100% of the variation in normal distribution would prevent any artificial thresholding due to inherent intensity fluctuations in a local window. We found that nine times the average standard deviation value to be sufficient, or a full-width of $18 \times 0.847 = 15.2$ for Sample 2; therefore, DCT = 15 for Sample 2.

Binary images, acquired using Bernsen's threshold and two automatic global thresholding methods (Otsu's method and Yen's method) [35,36], were generated from an image where the non-local means filter was already applied, and compared in Fig. 11. The first global threshold (Otsu's method) did not always accurately preserve the pore structure, especially for the small pores at the edge of the sample. The second global threshold (Yen's method) did not threshold the edges of the data due to the non-uniformity of intensity over the image, and the pores that were segmented were inaccurate in size, compared to the original image. On the other hand, Bernsen's local threshold provided clear thresholding at the edges as well as detection of lower contrast pores.

The difficulties of applying a local thresholding algorithm are often related to a lack of understanding of the user-defined parameters and how to properly choose the parameters. In this paper, Bernsen's method was chosen as an example, but different local thresholding techniques may also work provided that the user understands the algorithm correctly and chooses the parameters properly based on information in the images themselves.

Turning now to the five image sets, in each case we applied a 3D median filter ($3 \times 3 \times 3$) and a non-local means filter (Search window size: 21 pixels, Local neighborhood: 5 pixels, and similarity value: 0.6) [33] available in the Avizo software package [37] prior to applying the thresholding algorithm. The non-local means filter was applied in 2D for each reconstructed slice. A 3D median filter is a non-linear digital filter which replaces a voxel value with the median voxel value of the sub-volume ($3 \times 3 \times 3$) surrounding the targeted voxel. The filter is effective with removing speckle noise. A non-local means filter is an advanced denoising filter, which is very effective with reducing noise while preserving edges. Unlike local mean filters such as a median filter, the non-local means filter takes a mean of all pixels in the image, weighted by the similarity of the pixels to the target pixel, when applied in 2D. In the current implementation, the algorithm compares the neighborhoods of all pixels in a given search window with the neighbors of the targeted voxels. The similarity between the neighbors determines the weight with which the value of a voxel in the search window will influence the new value of the current voxel. The final weights are determined by applying a Gauss kernel to the similarity values. The reduction of noise level (gray scale standard deviation) allows the use of a smaller DCT value in Bernsen's method, which allows detection of smaller pores with lower image contrast.

The image processing algorithm and steps for all five image sets are shown in Table 4. Different image sets had different levels of noise fluctuation, which affected the standard deviation of the gray scale histograms and the required DCT values. An example of the results obtained after applying the image processing sequence and Bernsen's local thresholding algorithm to a Sample 2 image is shown in Fig. 12. The image processing steps (a median 3D filter and a non-local means filter) progressively reduced noise in the image, and the Bernsen's algorithm successfully thresholded smaller pores and what could be, in 2D, the remnant of a trapped powder particle within a larger pore. Based on these image analysis techniques, we can now go on to extract more quantitative phase information from the images.

5. Results: quantitative

5.1. Porosity, pore size distribution, and pore shape

Porosity values were measured for Samples 2–6 from the segmented images. The porosity values were compared to those obtained with a gravimetric method in Table 5. The porosity measured in this section includes the effect of trapped powders. Uncertainty values shown in Table 5 were estimated based on choosing a range of ±3 for the DCT values used, which we believe to be a conservative estimate of error associated with DCT determination. The resulting uncertainty of porosity measurement, as shown in Table 5, is fairly small and is less than the uncertainties associated with other conventional techniques [9]. The porosity values computed from XCT were comparable to those obtained based on a gravimetric method. The differences between gravimetric measurements and XCT measurements were possibly due to the XCT's finite resolution limit, the small cylindrical sample statistically varying from the bulk disk sample (this was seen for several cylindrical samples from the same disk in Slotwinski et al. [9]), and the limited local tomography region of interest used. The gravimetric method assumes a perfect disk shape geometry for the volume computation, which, along with the measured disk mass and nominal density of the CoCr alloy, were used to compute the porosity, as shown in Table 5. Similar gravimetric measurements

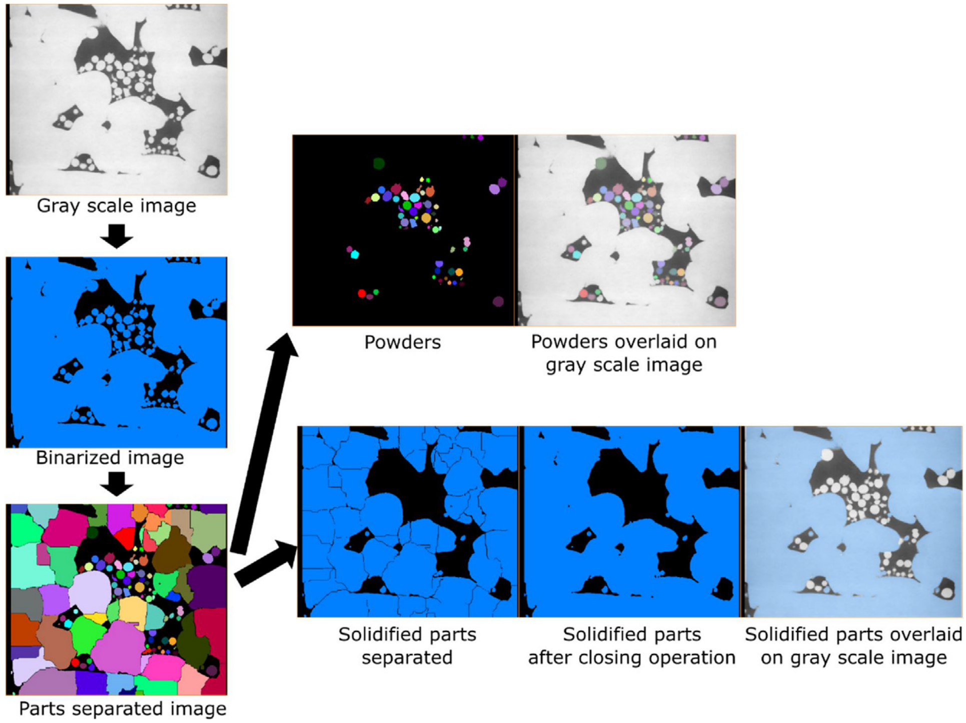

Fig. 26. Image processing steps to remove trapped powders.

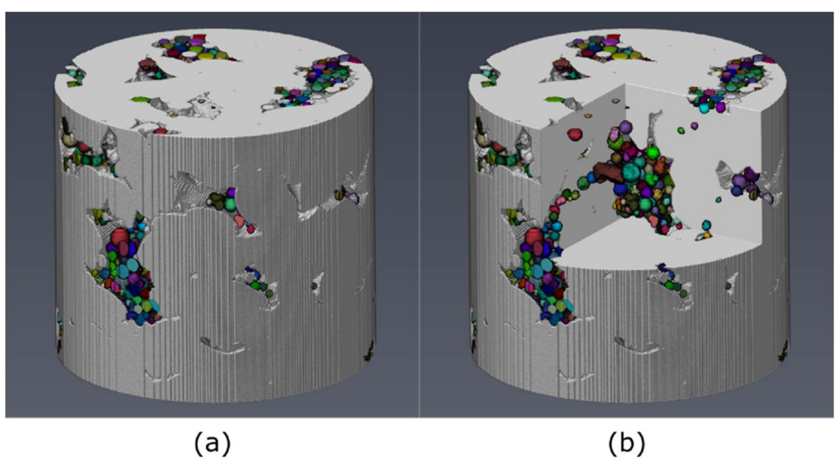

Fig. 27. Example 3D images of solidified part and trapped powders of Sample 5 (high-res).

Table 4
Image processing algorithms used.

	Image processing	Thresholding
Sample 2	Median 3D (3 × 3 × 3) Non-local means	Bernsen's method (r = 5 pixels, DCT = 15)
Sample 3	Median 3D (3 × 3 × 3) Non-local means	Bernsen's method (r = 5 pixels, DCT = 15)
Sample 4	Median 3D (3 × 3 × 3) Non-local means	Bernsen's method (r = 5 pixels, DCT = 21)
Sample 5	Median 3D (3 × 3 × 3) Non-local means	Bernsen's method (r = 5 pixels, DCT = 13)
Sample 6	Median 3D (3 × 3 × 3) Non-local means	Bernsen's method (r = 5 pixels, DCT = 17)

were performed by Slotwinski et al. [9], and, for Sample 2, they found a porosity of 2.44% for the disk and 1.10% for the cored cylinder, which shows how the porosity can vary across the original disk sample.

Individual pore sizes and shapes are critical for understanding the source of mechanical failure. The pore size distribution provides information on how the size of individual pores are distributed. Samples 2 and 4 have closed pores while Samples 3, 5 and 6 have a number of pores connected with each other. The concept of a pore size distribution is only well-defined for isolated pores; for connected pores, it depends on the measurement method used. Pore size distributions were measured for Samples 2 and 4 using Avizo software after labeling individual pores. The effect of DCT values on the differential and cumulative pore size distributions is shown in Fig. 13 for Sample 2, where the vertical axis is the actual number of individual pores. There were very few pores larger than 0.06 mm

Table 5
Porosity of cored cylinders as measured with XCT, along with porosity determined by mass and volume measurements.

	Disk porosity	Porosity[a]	2σ error	Porosity[b]	Uncertainty
Sample 2	1.4%	1.1%	0.06%	1.00%	±0.09%
Sample 3	18.1%	[c]	[c]	19.03%	±0.115%
Sample 4	2.1%	1.1%	0.06%	0.42%	±0.0235%
Sample 5	10.2%	13.73%	0.77%	10.90%	±0.04%
Sample 6	72.0%	[c]	[c]	74.56%	±0.085%

[a] Mass/volume measurements of cored cylinders by Slotwinski et al. [9].
[b] Porosity of cored cylinders measured by CT.
[c] Not measured.

Table 6
Global porosity, standard deviation of CT z-layer porosity measurements based on XCT, and standard deviation normalized by the global porosity.

	Porosity (%)	Standard deviation of z-layer porosity (%)	Standard deviation/global porosity
Sample 2	1.00	0.278	0.28
Sample 3	19.03	2.712	0.14
Sample 4	0.42	0.0966	0.23
Sample 5	10.90	1.234	0.11
Sample 6	74.56	4.000	0.054

Table 7
Global porosity and standard deviation (std) of CT slice-wise porosity measurements in the x, y, and z directions, based on 684 × 684 × 900 voxel sub-samples.

	Porosity (%)	z-slice std (%)	y-slice std (%)	x-slice std (%)
Sample 2	0.97	0.31	0.13	0.13
Sample 3	18.91	3.03	0.62	0.66
Sample 4	0.44	0.12	0.12	0.13
Sample 5	10.78	1.41	1.31	1.36
Sample 6	74.40	4.01	4.78	1.52

and less than the maximum of 0.1 mm, and so the graph only goes to 0.06 mm so as to better see the detail at lower pore sizes. Recall from Table 4 that DCT = 15 was taken to be the best value for Sample 2, and the uncertainty listed in Table 5 came from varying DCT by ±3, which is the range shown in Fig. 13. Values of the Equivalent Spherical Diameter (ESD) were computed by equating the volume of a perfect sphere to the voxel volume of a pore (V_p), as shown in Eq. (2). As the DCT value increased, fewer smaller pores were detected, dropping the distribution in the small pore region, but the detectability of the larger pores was not affected. The pore size distribution of Samples 2 and 4 are compared in Fig. 14, graphed in the same manner as Fig. 13 and for the best DCT value given in Table 4. Larger number of pores were identified in Sample 2 contributing to the larger porosity value while the average pore sizes were still similar to each other for both samples based on the value of D_{50} measured from the cumulative pore size distribution curves of Fig. 14.

$$ESD = \left(6\frac{V_p}{\pi}\right)^{\frac{1}{3}} \quad (2)$$

For Sample 2, which had porosity of about 1%, a total of 10 938 pores were detected. The largest pore had a volume of $5.06038 \cdot 10^{-4}$ mm^3, which is equivalent to a spherical diameter of 99 μm. The location and shape of this pore are shown in Fig. 15a and b, respectively. The shape of the pore is far from spherical, and a high stress concentration is expected around this pore, if the sample were to be mechanically loaded normal to the plane of the pore or parallel to the build direction, since this particular pore is also generally aligned parallel to the AM layers.

The shape of a pore can be quantified by measuring a shape parameter (one of many, e.g [38]), defined in Eq. (3), where $A_{surface}$ is the surface area of the pore and V is the voxel-based pore volume. $A_{surface}$ is measured based on the Cauchy formula that relates perimeter and the number of intercepts, which provides a more realistic surface area of the pore than by simply counting voxel faces [39]. The shape parameter has a value of 1 for a perfect sphere, and the value increases for less spherical pores. The calculation is implemented in Avizo (using *shapeVA3d*). Based on the shape parameter and pore volume measures, the shapes and sizes of the pores were correlated. Fig. 16d shows that the shape parameter increased approximately quadratically with the equivalent spherical diameter of the pore, so that as pores increased in size they became less spherical. Only pores larger than 125 voxels in volume were used for the analysis to achieve a more reliable measurement of $A_{surface}$. To define a particle shape adequately, 5 or 10 voxels across one linear dimension is generally needed [40]. Example images of the pore shapes are shown in Fig. 16a, b, and c, respectively, for three widely different pore sizes.

$$ShapeParameter = \frac{\left(A_{surface}{}^{3}\right)}{36\pi V^2} \quad (3)$$

5.2. Variation of porosity with and across the build direction

While the 3D porosity value provides a global indication for the sample volume studied, and the pore size distribution indicates what size pores make up the pore space, the local variation of the porosity in a given direction is also interesting. The AM process considered here is a layered process, so the variation of porosity in the z-direction (build direction) could be relevant to the process. The variation of porosity over the height (z-layer) was measured for each CT slice, as shown in Fig. 17, using the properly segmented images. The dotted lines represent the global 3D porosity value computed based on the XCT measurements. Large variations can be seen compared to the global porosity values.

The standard deviations of the z-layer porosity values over the height are shown in Table 6 for Samples 2–6. The standard deviation values show how the porosity fluctuates from layer to layer in the z-direction. The last column of Table 6 shows the standard deviation of the porosity relative to the global porosity. Samples 2 and 4 have the lowest porosities yet the highest values of standard deviation relative to their porosity. Samples 3 and 5 are similar, with a lower relative value of standard deviation, while Sample 6 has the highest global porosity and the lowest standard deviation relative to porosity. These results may seem counter-intuitive. A thought example may help. Suppose we had a sample with a single cylindrical pore that was aligned along the build direction all the way from the bottom to the top of the sample. Then no matter how large that pore was, the standard deviation of the porosity, as calculated in layers normal to the build direction, would be zero,

Table 8
Bernsen threshold parameters and analysis results of Sample 3 high-res and Sample 5 high-res.

	r (pixel)	DCT	Volume (mm^3)	Porosity (%)	Porosity without trapped particles (%)	Number of trapped particles
Sample 3 high-res	5	48	0.404	17.3	19.1	506
Sample 5 high-res	5	16	0.400	11.2	14.6	818

since the porosity would not be changing from layer to layer. Since Samples 2 and 4 have smaller and isolated pores, there is relatively more change from layer to layer. Samples 3, 5, and 6 have porosity that is more connected from layer to layer, and therefore a smaller relative standard deviation.

The AM process considered here had a height per layer of nominally 20 μm. Judging by the XCT voxel sizes used in Table 2, for the lower resolution scans, there are about eight XCT layers for every build layer. In fact, there were about 100+ build layers per stack of XCT images for all five samples considered (see Table 2). Therefore, perhaps computing the porosity over each XCT slice is too fine a resolution to see any connection to the build process. As well, from the discussion of Fig. 5 for Sample 5, since four different laser tracks can be seen in the one cross-sectional image, averaging over $4 \times 8 = 32$ XCT slices could also be better connected to the actual build process. Therefore, we took the porosity per XCT layer data and performed a running average, where the porosity of each slice was replaced with the average of the porosity in the next eight or 32 slices, including itself. Fig. 18 shows all three curves, for 1, 8, and 32 slice averaging, on the same graph, for Sample 2. The 8-slice average looks nearly identical to the 1-slice data, so that the variation of porosity over the build scale matches that over the XCT scale. The 32-slice average data is different, however, and smoother, yet it still shows significant variation over the sample height.

The results for Sample 4 were similar to those of Sample 2, and the results for Sample 5 were similar to those of Sample 3, so only results for Samples 3 (Fig. 19) and Sample 6 (Fig. 20) are presented. One difference that can be seen between the graph for Sample 2, Fig. 18, and that for Sample 3, Fig. 19, are that the peak-to-peak distance for the latter sample was larger than those for Sample 2. This is a reflection of the pore size. Consider a sample with several cubic pores, aligned with the build direction, of different sizes and which did not overlap in any plane. A height-porosity graph would show several square-wave peaks to the right, towards higher porosity, and each peak would correspond to one pore. The width of each square-wave peak would be equal to the edge length of the corresponding cubic pore. Larger cubic pores would correspond to wider peaks. The smaller peak-to-peak distance for Sample 2 is because that sample has smaller pore sizes than does Sample 3. Fig. 20, for Sample 6, has even larger peak-to-peak distances, indicative of the large pores seen in this sample.

To gain better understanding of the previous results, a numerical simulation model was used to generate similar data. This digital model was a cube of size 1000^3 cubic voxels, similar to those used in other applications [41]. Three versions of the model were used, focusing on Sample 2. In the first, each voxel was randomly either pore or solid, with the total porosity equal to 0.01, the same as in Sample 2. The second model had monosize non-overlapping spherical pores randomly distributed over the volume, made from voxels, with again the total porosity equal to 0.01. The diameter of the pores was varied. The third model had a distribution of spherical pore diameters, approximately equal to the size distribution shown in Fig. 14, with one voxel equaling 2.44 μm, similar to the Sample 2 images, and almost the same number of pores, 10 787 vs. the experimental value of 10 938.

Fig. 21 shows the porosity results for such a model of Sample 2, which used monosize spheres of diameter 61 μm. Qualitatively, these results look very similar to those of Fig. 18. There is very little difference between the 1-layer and 8-layer averages, while the 32-layer average is significantly smoother and has less horizontal variation. Since the model was built with pores that were not correlated in any way, except that they were required to be non-overlapping, it seems clear that the variation seen in Fig. 18 is not indicative of any variation in the process control but rather is simply a reflection of the random pore geometry.

An additional way of looking at these graphs is to consider how the standard deviation of the porosity over z-layers changes when increasingly higher number of layers are averaged over, as was done earlier to better connect to actual build distances. Of course, this standard deviation must go to zero when the number of layers averaged over, in the running average, equals the total number of slices in the XCT sample. Fig. 22 shows how this standard deviation changes with the number of layers in the running average, for the Sample 2 experimental data ("exp', Fig. 22) and for several models of Sample 2. The models are the single voxel pore model ('voxel', Fig. 22), several diameter monosize spherical pore models ("61 μm", "37 μm", "27 μm", "17 μm", Fig. 22), and the model with the pore size distribution taken from Fig. 14 ("psd", Fig. 22). The experimental data forms the highest curve, even higher than the diameter = 61 μm monosize spherical pore model, indicating that the standard deviation is controlled mainly by the largest pores, since Fig. 14 indicated that most of the pores, by number, were much smaller than 61 μm. It is interesting that the one voxel pore model, with single voxel "pores" roughly 2.44 μm in diameter, had the smallest standard deviation at the start and quickly decreased with increasing number of layers in the running average, due to its small "pore" size being quickly averaged out.

The variation in the 1-layer (i.e., computing over each layer and no averaging) standard deviation is caused by the pore size, as can be clearly seen in Fig. 23, where the 1-layer standard deviations for the monosize spherical pore models, including the single voxel pore model, are plotted vs. pore sphere diameter. The graph is linear, and the slope of the fitted line, which is forced to go through the origin, is $3.092 \cdot 10^{-5}$, using the units of the figure.

To try to get an indication of what size pores were controlling the experimental data curve in Fig. 22, we can take the 1-layer standard deviation for the Sample 2 results, which is about 0.00275, and divide it by the slope of the line in Fig. 23, $3.092 \cdot 10^{-5}$, to get a pore size of about 89 μm, which is consistent with the larger pore sizes measured for Sample 2.

Analyzing the porosity over the layers in the build direction can give valuable information about the pore structure of the sample, at least for isolated pores. For the more connected pores of Samples 3, 5, and 6, we have been able to say less. However, for these samples, it is probable that these pores have a degree of anisotropy, being longer in the build direction [9]. It is therefore of interest to do the same kinds of computations as above but for the horizontal (x and y) directions. Since the image stack is cylindrical, we need to sub-sample the image stacks to get rectangular prisms to work with. A 684×684 square sub-sample was taken from each image, so that the rectangular prism that was finally worked with was $684 \times 684 \times 900$ voxels. The porosity standard deviation for the z-layers were recalculated for 900 684×684 pixel images, while the x and y layer porosity standard deviations were computed for 684×900 pixel images. Only the 1-layer standard deviations were computed and are given in Table 7. Comparing to Table 6, it can be seen that the global porosities found and the z-layer porosity standard deviations were slightly different for the smaller images. The reason is that a smaller sub-sample of the image stack was used, so the numbers changed slightly.

Note for Sample 3, the x and y-slice porosity standard deviations, which are quite similar, are much smaller than the z-slice porosity standard deviation, clearly implying anisotropy in pore size and/or randomness between the vertical and horizontal directions. This is clearly seen in Fig. 24, which shows the 1-slice porosities for the z, y, and x directions. For Samples 2 and 4, the x, y, and z direction porosity standard deviations are similar, implying that the small isolated pores in these samples are fairly isotropic in shape and in distribution. However, for Sample 2, the porosity standard deviation in the z-direction is larger than the other two directions. The porosity standard deviations for Samples 5 and 6, however, do not tell such a clear story. The Sample 5 porosity standard deviations seem much more isotropic that expected, compared to Sample 3, and for Sample 6, it is puzzling that the y-layer porosity standard deviation is much larger than for the x-layer values, and even is somewhat larger than the z-layer direction. Fig. 25 shows the z, y, and x direction porosities, which are quite different from each other and clearly are a result of the large anisotropy seen in the Sample 6 images.

5.3. Trapped powder

The samples produced with a large hatch spacing or a high scan speed exhibited trapped metal powders within the pore space (Samples 3, 5, and 6). These trapped powders provide little structural support in tension, since they are at best lightly sintered to the solid frame, but do contribute to the overall density measurement, so that using any strength-porosity empirical correlation from the literature will provide a somewhat inaccurate estimate of structural strength. An image processing technique was developed to visually remove powders from the image. The high-resolution (0.870 μm/voxel) Sample 3 and Sample 5 images were used for this analysis. A marker-based watershed separation algorithm (separate grain with marker size = 4) (Eddins et al. [42]. in Avizo was applied to the segmented images to break any connecting neck between neighboring powder particles as well as any connection between powder particles and the solid frame. The process not only breaks contacts points between grains, but can also, as an artifact, break solidified parts into smaller pieces. Knowing that the powder was approximately in the 5 μm to 60 μm size range, and that the particles were approximately spherical in shape [20], enabled constraints to be applied when apparent powder particles were chosen. Only those that were smaller than 60 μm in diameter and had a shape parameter value less than 2.4 were chosen. The overall image analysis processes are illustrated in Fig. 26. For Sample 5, the global porosity was measured to be 11.2% and 14.6% before and after removing the effect of trapped powders, respectively. The latter porosity should be used in any strength-porosity correlation formulas. The porosity measurement results vary slightly from those reported in Table 5 as different cylinders were used for the higher resolution measurements. The porosity and number of trapped powder particles are also shown in Table 8. Sample 5 had 818 powder particles and Sample 3 had 506 powder particles because Sample 5 had lower overall porosity but larger individual pore spaces. Example high-resolution 3D images of Sample 5 with and without trapped powders are shown in Fig. 27.

The size distribution of the trapped powders is shown in Fig. 28, by number. Only the powders that did not touch the cylindrical CT scan boundaries were chosen for the analysis, since particles that did touch the boundaries could have been artificially cut in the reconstruction process. Based on a Gaussian fit, the peak was obtained at an equivalent spherical diameter of 25.6 μm for both samples. Based on the cumulative powder size distribution curve, D_{50} was found to be about 25.1 μm for Sample 5 and 24.3 for Sample

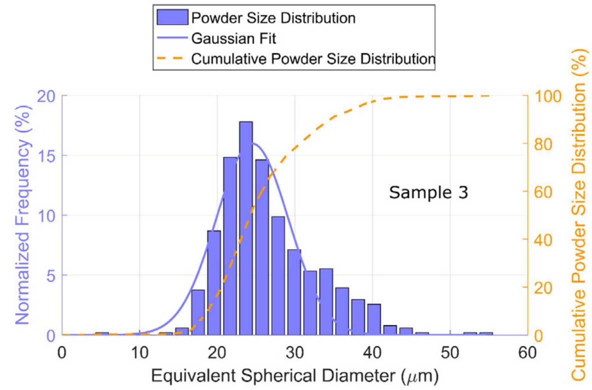

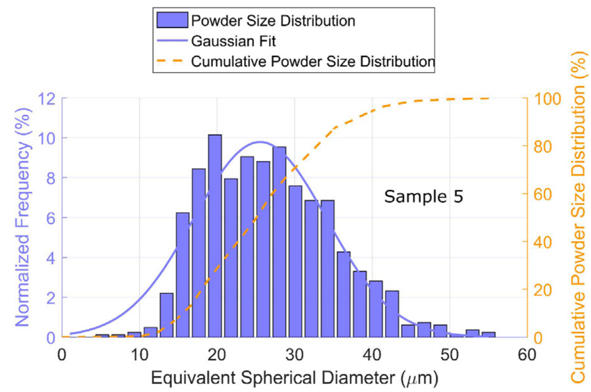

Fig. 28. Number fraction-based particle size distribution for powder particles trapped in the pores of Samples 3 and 5, analyzed at a voxel size of 0.870 μm.

3. The CoCr virgin powder studied in Slotwinski et al. [20], which was nominally the same as was used to produce these samples, was found to have a value of about D_{50} = 26 μm, as measured by XCT in terms of number (the value given in Slotwinski et al. [20] was by mass), in close agreement with the present result. The size range of the trapped powders, as indicated in Fig. 28, was about 5 μm to 55 μm, while the XCT results from [20] indicated a size range of 15 μm to about 80 μm, again in reasonable agreement. The XCT results from Slotwinski et al. [20] did not consider particles smaller than about 15 μm, hence the disagreement at the lower size range, but the laser diffraction results from that paper did see particle down to a few micrometers in size. The absence of particles larger than 55 μm and less than 80 μm could be because such larger particles would have had more chance to touch more than one solid frame surface, and so were less likely to be detached by the watershed algorithm

For most structural parts, there is no trapped powder because the built parts are close to theoretical density and the only pores present are too small to contain powder. However, if builds were to be produced with a controlled larger porosity and pore structure, say for a medical implant, the matter of trapped powder in the pores must be dealt with. Pores that are larger than the minimum powder size used will almost surely contain trapped powder, so to achieve controlled smaller pores requires smaller powder particles.

6. Summary and conclusions

High-resolution XCT scans of additively manufactured CoCr specimens were acquired to understand the effect of processing parameters on pore structure formation and global porosity, to produce qualitative information relevant to the build process, to demonstrate image processing techniques that are necessary to achieve quantitative information about the pore structure, and then to use these techniques to produce quantitative pore structure information.

The image processing and segmentation steps used in this paper were:

- Step 1: Noise filtering (median 3D and non-local means filters).
- Step 2: (optional) Image rescaling to adjust the image intensity of the solid phase to be over 128 (for 8-bit images) for a suitable application of the Bernsen local thresholding method.
- Step 3: Measurement of the average standard deviation for the metal phase in the homogenous areas of the XCT data from five locations in a single XCT slice for three different non-adjacent XCT slices. Eighteen times the measured standard deviation should be used for the value of DCT in the Bernsen local thresholding algorithm.
- Step 4: Application of the Bernsen local thresholding method using the computed value of DCT.

The major conclusions of this paper are the following:

- XCT images of CoCr alloy samples produced with different AM processing parameters (scan speed and hatch spacing) but the same energy density achieved similar global porosities, but very different pore structure, which could include trapped powder particles in the larger pores.
- To obtain quantitative results, the most crucial step was to segment an image into a binary image of pores and solid metal. The XCT images were thresholded based on image processing filters (median 3D and non-local means) and an automatic local thresholding algorithm (Bernsen's method), whose parameters were estimated based on the standard deviation of the gray scale in local windows in the images. This method gave far better results than did global thresholds and is suggested to serve as a basis for image processing standards for these materials. This combination of image analysis techniques could serve as a basis for delineating standard XCT/image analysis methods for AM materials. Porosities measured based on the thresholded XCT images were close to those measured gravimetrically. Differences were due to different measurement techniques, and different size samples, which coupled to the local variation of porosity within the entire samples.
- The large hatch spacing of Sample 5 allowed the visualization of the 67° hatch rotation scheme clearly in the pore structure. The hatch width was measured to be larger than the laser spot size. The vertical and horizontal XCT slices around a hatch revealed the hatch thickness was about 4–5 x the AM layer thickness (80–100 μm).
- For the closed pore samples (Samples 2 and 4), pore size distributions were measured. Correlations between the pore size and shapes were carried out, and a shape parameter, formed out of the surface area and volume of each pore, was found to increase approximately quadratically with the equivalent spherical diameter of the pore, so that larger pores were less spherical than smaller pores, on average.
- Porosity as function of height was analyzed based on the processed XCT data. The variation of porosity over the build direction of the sample was characterized by the computed standard deviation for both the XCT experimental results and simulated pore structures with non-overlapping spheres. Due to comparison of experimental to random model results, the porosity variation in the AM samples was found to be an inherent characteristic of the random pore structure rather than reflecting on the manufacturing process. The porosity standard deviation for 1-layer averaging was shown to linearly increase with maximum pore size. Performing a running average over eight XCT slices (approximately 20 μm or a build layer) for the measurement of porosity variation made little difference compared to only performing a 1-layer average over the XCT slice thickness. Averaging over 32 slices, which was approximately four AM build layers, significantly smoothed and reduced the porosity variation with height, agreeing with image evidence seen of four different build tracks in a cross-sectional XCT slice.
- Porosity variation in the horizontal directions (x and y) were further compared to porosity variation in the vertical direction (z). The closed pore samples, Samples 2 and 4, had similar porosity standard deviation in the x, y, and z direction, implying that the small isolated pores in these samples were fairly isotropic in shape and in distribution. For Sample 3, the x and y-slice porosity standard deviations were much smaller than the z-slice porosity standard deviation, clearly implying anisotropy in pore size and/or randomness between the vertical and horizontal directions.
- An image processing procedure was developed to computationally remove any trapped powder particles, so that the new porosity was better related to mechanical properties. Being able to remove the trapped powder particles enabled their particle size distribution to be computed based on the XCT images. The value of D_{50} of the trapped powders (25 μm) compared well to that of the virgin powders measured from a previous study (D_{50} = 26 μm).

Acknowledgements

The authors greatly appreciate the efforts of Dustin E. Lindley (Morris Technologies, now University of Cincinnati Research Institute) in producing the reference samples and helping us understand the relationship between process parameters and porosity.

References

[1] M. Tang, P.C. Pistorius, J.L. Beuth, Prediction of lack-of-fusion porosity for powder bed fusion, Addit. Manuf. 14 (2017) 39–48, http://dx.doi.org/10.1016/j.addma.2016.12.001.
[2] G.K.L. Ng, A.E.W. Jarfors, G. Bi, H.Y. Zheng, Porosity formation and gas bubble retention in laser metal deposition, Appl. Phys. A 97 (3) (2009) 641–649, http://dx.doi.org/10.1007/s00339-009-5266-3.
[3] J.M. Wentzell, Metal powder production by vacuum atomization, J. Vac. Sci. Technol. 11 (6) (1974) 1035–1037, http://dx.doi.org/10.1116/1.1318676.
[4] H.F. Fischmeister, A.D. Ozerskii, L. Olsson, Solidification structure of gas-atomized high-speed steel powders, Powder Metall. 25 (1) (1982) 1–9, http://dx.doi.org/10.1179/pom.1982.25.1.1.
[5] R. Gerling, R. Leitgeb, F.P. Schimansky, Porosity and argon concentration in gas atomized γ-TiAl powder and hot isostatically pressed compacts, Mater. Sci. Eng.: A 252 (2) (1998) 239–247, http://dx.doi.org/10.1016/s0921-5093(98)00656-x.
[6] M.N. Ahsan, R. Bradley, A.J. Pinkerton, Microcomputed tomography analysis of intralayer porosity generation in laser direct metal deposition and its causes, J. Laser Appl. 23 (2) (2011) 022009, http://dx.doi.org/10.2351/1.3582311.
[7] L.E. Murr, S.M. Gaytan, A. Ceylan, E. Martinez, J.L. Martinez, D.H. Hernandez, B.I. Machado, D.A. Ramirez, F. Medina, S. Collins, R.B. Wicker, Characterization of titanium aluminide alloy components fabricated by additive manufacturing using electron beam melting, Acta Mater. 58 (5) (2010) 1887–1894, http://dx.doi.org/10.1016/j.actamat.2009.11.032.
[8] H. Gong, K. Rafi, H. Gu, G.D. Janaki Ram, T. Starr, B. Stucker, Influence of defects on mechanical properties of Ti-6Al-4V components produced by selective laser melting and electron beam melting, Mater. Des. 86 (2015) 545–554, http://dx.doi.org/10.1016/j.matdes.2015.07.147.
[9] J.A. Slotwinski, E.J. Garboczi, K.M. Hebenstreit, Porosity measurements and analysis for metal additive manufacturing process control, J. Res. Nat. Inst. Stand. Technol. 119 (2014) 494–528, http://dx.doi.org/10.6028/jres.119.019.
[10] A.B. Spierings, M. Schneider, R. Eggenberger, Comparison of density measurement techniques for additive manufactured metallic parts, Rapid Prototyp. J. 17 (5) (2011) 380–386, http://dx.doi.org/10.1108/13552541111156504.
[11] S. Torquato, Random Heterogeneous Materials: Microstructure and Macroscopic Properties, Springer-Verlag, New York, 2002.
[12] E. Todorov, R. Spencer, S. Gleeson, M. Jamshidinia, S.M. Kelly, America Makes: National Additive Manufacturing Innovation Institute (NAMII) Project 1: Nondestructive Evaluation (NDE) of Complex Metallic Additive Manufactured (AM) Structures, 2014 http://www.dtic.mil/cgi-bin/GetTRDoc?Location=U2&doc=GetTRDoc.pdf&AD=ADA612775.

[13] E. Maire, P.J. Withers, Quantitative X-ray tomography, Int. Mater. Rev. 59 (1) (2014) 1–43, http://dx.doi.org/10.1179/1743280413y.0000000023.
[14] F.H. Kim, D. Penumadu, J. Gregor, N. Kardjilov, I. Manke, High-resolution neutron and X-ray imaging of granular materials, J. Geotech. Geoenviron. Eng. 139 (5) (2013) 715–723, http://dx.doi.org/10.1061/(ASCE)GT.1943-5606.0000809.
[15] W.B. Lindquist, A. Venkatarangan, J. Dunsmuir, T.f. Wong, Pore and throat size distributions measured from synchrotron X-ray tomographic images of Fontainebleau sandstones, J. Geophys. Res.: Solid Earth 105 (B9) (2000) 21509–21527, http://dx.doi.org/10.1029/2000jb900208.
[16] K. Natesaiyer, C. Chan, S. Sinha-Ray, D. Song, C.L. Lin, J.D. Miller, E.J. Garboczi, A.M. Forster, X-ray CT imaging and finite element computations of the elastic properties of a rigid organic foam compared to experimental measurements: insights into foam variability, J. Mater. Sci. 50 (11) (2015) 4012–4024, http://dx.doi.org/10.1007/s10853-015-8958-4.
[17] J. Kastner, B. Harrer, H.P. Degischer, High resolution cone beam X-ray computed tomography of 3D-microstructures of cast Al-alloys, Mater. Charact. 62 (1) (2011) 99–107, http://dx.doi.org/10.1016/j.matchar.2010.11.004.
[18] G. Nicoletto, R. Konečná, S. Fintova, Characterization of microshrinkage casting defects of Al-Si alloys by X-ray computed tomography and metallography, Int. J. Fatigue 41 (2012) 39–46, http://dx.doi.org/10.1016/j.ijfatigue.2012.01.006.
[19] E. Girardin, C. Renghini, J. Dyson, V. Calbucci, F. Moroncini, G. Albertini, Characterization of porosity in a laser sintered MMCp using X-ray synchrotron phase contrast microtomography, Mater. Sci. Appl. 02 (09) (2011) 9, http://dx.doi.org/10.4236/msa.2011.29180.
[20] J.A. Slotwinski, E.J. Garboczi, P.E. Stutzman, C.F. Ferraris, S.S. Watson, M.A. Peltz, Characterization of metal powders used for additive manufacturing, J. Res. Nat. Inst. Stand. Technol. 119 (2014) 460–493, http://dx.doi.org/10.6028/jres.119.018.
[21] L. Thijs, F. Verhaeghe, T. Craeghs, J.V. Humbeeck, J.-P. Kruth, A study of the microstructural evolution during selective laser melting of Ti-6Al-4V, Acta Mater. 58 (9) (2010) 3303–3312, http://dx.doi.org/10.1016/j.actamat.2010.02.004.
[22] B. Vandenbroucke, J.P. Kruth, Selective laser melting of biocompatible metals for rapid manufacturing of medical parts, Rapid Prototyp. J. 13 (4) (2007) 196–203, http://dx.doi.org/10.1108/13552540710776142.
[23] S. Cho, J. Bian, C.A. Pelizzari, C.-T. Chen, T.-C. He, X. Pan, Region-of-interest image reconstruction in circular cone-beam microCT, Med. Phys. 34 (12) (2007) 4923–4933, http://dx.doi.org/10.1118/1.2804924.
[24] E.J. Garboczi, K.A. Snyder, J.F. Douglas, M.F. Thorpe, Geometrical percolation threshold of overlapping ellipsoids, Phys. Rev. E 52 (1) (1995) 819–828.
[25] E.E. Underwood, Quantitative Stereology, Addison-Wesley Pub. Co., Reading, Mass, 1970.
[26] R. Li, J. Liu, Y. Shi, L. Wang, W. Jiang, Balling behavior of stainless steel and nickel powder during selective laser melting process, Int. J. Adv. Manuf. Technol. 59 (9) (2012) 1025–1035, http://dx.doi.org/10.1007/s00170-011-3566-1.
[27] J.P. Kruth, G. Levy, F. Klocke, T.H.C. Childs, Consolidation phenomena in laser and powder-bed based layered manufacturing, CIRP Ann.—Manuf. Technol. 56 (2) (2007) 730–759, http://dx.doi.org/10.1016/j.cirp.2007.10.004.
[28] I. Yadroitsev, L. Thivillon, P. Bertrand, I. Smurov, Strategy of manufacturing components with designed internal structure by selective laser melting of metallic powder, Appl. Surf. Sci. 254 (4) (2007) 980–983, http://dx.doi.org/10.1016/j.apsusc.2007.08.046.
[29] J.C. Russ, The Image Processing Handbook, CRC, Press, Inc., 1992.
[30] M. Sezgin, B.l. Sankur, Survey over image thresholding techniques and quantitative performance evaluation, J. Electron. Imaging 13 (1) (2004) 146–168, http://dx.doi.org/10.1117/1.1631315.
[31] J. Bernsen, Dynamic Thresholding of Grey-level Images, International Conference on Pattern Recognition, Paris, France, 1986, pp. 1251–1255.
[32] C.A. Schneider, W.S. Rasband, K.W. Eliceiri, NIH Image to ImageJ: 25 years of image analysis, Nat. Methods 9 (7) (2012) 671–675.
[33] A. Buades, B. Coll, J.-M. Morel, Non-local means denoising, Image Process. Line 1 (2011), http://dx.doi.org/10.5201/ipol.2011.bcm_nlm.
[34] P. Behnel, T. Wagner, Non Local Means Denoise v1.4.6, 2016.
[35] J.-C. Yen, F.-J. Chang, S. Chang, A new criterion for automatic multilevel thresholding, IEEE Trans. Image Process. 4 (3) (1995) 370–378, http://dx.doi.org/10.1109/83.366472.
[36] N. Otsu, A threshold selection method from gray-level histograms, IEEE Tran. Syst. Man Cybern. 9 (1) (1979) 62–66, http://dx.doi.org/10.1109/tsmc.1979.4310076.
[37] Avizo 9.0, Thermo Fisher Scientific, Waltham, MA.
[38] M.A. Taylor, E.J. Garboczi, S.T. Erdogan, D.W. Fowler, Some properties of irregular 3-D particles, Powder Technol. 162 (1) (2006) 1–15, http://dx.doi.org/10.1016/j.powtec.2005.10.013.
[39] J. Serra, Image Analysis and Mathematical Morphology, Academic Press, 1982.
[40] E.J. Garboczi, Three-dimensional mathematical analysis of particle shape using X-ray tomography and spherical harmonics: application to aggregates used in concrete, Cem. Concr. Res. 32 (10) (2002) 1621–1638, http://dx.doi.org/10.1016/s0008-8846(02)00836-0.
[41] E.J. Garboczi, Percolation phase diagrams for multi-phase models built on the overlapping sphere model, Physica A 442 (2016) 156–168, http://dx.doi.org/10.1016/j.physa.2015.09.014.
[42] S.L. Eddins, R.C. Gonzalez, R.E. Woods, Digital Image Processing Using Matlab, Princeton Hall Pearson Education Inc., New Jersey, 2002.